Selective clast survival in an experimentally-produced pseudotachylyte

Simone Papa [a,*], Elena Spagnuolo [b], Giulio Di Toro [a,b], Andrea Cavallo [c], Marco Favero [a], Alfredo Camacho [d], Giorgio Pennacchioni [a]

[a] Department of Geosciences, University of Padova, Via Gradenigo 6, Padua, Italy

[b] Istituto Nazionale di Geofisica e Vulcanologia, Via di Vigna Murata 605, Rome, Italy

[c] CERTEMA S.c.a.r.l., S.P. del Cipressino km 10, Cinigiano, Italy

[d] Department of Geological Sciences, University of Manitoba, 125 Dysart Road, Winnipeg, Canada

[*] Corresponding author

E-mail addresses: simone.papa@unipd.it[*] (+393496059117), elena.spagnuolo@ingv.it, giulio.ditoro@unipd.it, a.cavallo@laboratoriotecnologicogrosseto.it, marco.favero@unipd.it, alfredo.camacho@umanitoba.ca, giorgio.pennacchioni@unipd.it.

Keywords: pseudotachylyte, laboratory earthquake, rotary-shear apparatus, frictional melting, clast size distribution, thermal shock

Highlights

- Clast survival to melting of natural pseudotachylytes reproduced experimentally
- Clast survival depends on mineral melting temperature and thermal shock resistance
- Preferential melting of garnet clasts is enhanced by thermal shock comminution

- For large earthquakes, frictional sliding and heating control clast survival

Abstract

On-fault processes during earthquakes contribute to seismic rupture propagation and slip. Here we investigate clast fragmentation in an experimental pseudotachylyte (solidified seismic melt) produced with a rotary-shear machine. We slid for 0.44 m (corresponding to Mw ≥ 6 earthquakes), at slip rates > 1 m/s, pre-cut samples of quartz + phyllosilicates + plagioclase + sillimanite + garnet -bearing ultramylonite, that hosts pseudotachylytes in nature. The ultramylonite minerals extensively preserved as clasts in the experimental pseudotachylyte are quartz, plagioclase, and sillimanite. Garnet is scarcely preserved, despite having a melting temperature similar to plagioclase, probably due to having low thermal shock resistance. This selective clast survival is identical to the one found in the natural pseudotachylytes.

Based on these experimental observations and assuming non-equilibrium melting, the preservation of a mineral, as a clast, in the melt appears to be controlled by its thermal shock properties as well as by its melting temperature. Since the mechanical effects of rupture propagation in these experiments were negligible, we conclude that, for Mw ≥ 6 earthquakes, (i) frictional slip and heating of the slipping zone plus (ii) thermomechanical properties of minerals, rather than fault rupture processes, control mineral comminution and clast survival in frictional melts.

1. Introduction

On-fault coseismic deformation processes are triggered by the propagation of the rupture tip at ~ km/s followed by frictional sliding at ~ m/s (Heaton, 1990; Scholz, 2019). In crystalline basement rocks, rupture propagation and seismic slip along a fault may result in the production of frictional melts (pseudotachylytes once solidified; Maddock, 1974; Sibson, 1975). Seismic melts develop immediately after slip initiation (few milliseconds: Violay et al., 2014) and are interpreted to form by non-equilibrium melting of the minerals in the host rock (Spray, 1987; Maddock, 1992; O'Hara, 1992). In fact, minerals with a low-melting-point, such as phyllosilicates, are commonly completely consumed during melting, whereas high-melting-point minerals, such as quartz, survive as clasts within pseudotachylytes as was already observed by Shand (1916). Mineral comminution is an essential process leading to and favouring frictional melting by increasing the mineral surface area (Wenk, 1978; Magloughlin, 1989; Spray, 1995). During coseismic slip, both mechanical and thermal processes contribute to comminution (Spray, 1992). Spray (1992; 2010) proposed that the minerals with lower fracture toughness and thermal shock resistance are more susceptible to comminution and more readily disappear in the frictional melt, if the melt temperature reaches their melting point. Papa et al. (2018) proposed a model to calculate the thermal shock resistance of minerals and the results are consistent with the relative amount of clasts observed in natural pseudotachylytes of the Mont Mary unit (Western Alps). However, this model disregards the effects related to propagation of the earthquake rupture tip with associated process/damage zone that can induce significant comminution preceding frictional melting (Petley-Ragan et al., 2019; Incel et al., 2019). The individual contributions to comminution of rupture related processes and thermal effects during seismic slip are unknown.

This study examines the response of different minerals to frictional melting by documenting the survival of clasts in experimental pseudotachylyte produced in a rotary shear machine. The experiment was performed by sliding the bare sawed surfaces of two hollow cylinders drilled from Mont Mary ultramylonite that host natural pseudotachylytes. This experimental configuration minimises the effects associated with seismic rupture propagation which is dramatic in natural faults causing instantaneous changes in stress eigenvalues (up to several GPa's) and abrupt rotation of the stress eigenvectors (Reches and Dewers, 2005; Di Toro et al., 2005; Okubo et al., 2019). As a result, clast formation and survival in the experimental fault can be mainly attributed to the stage of frictional seismic slip. The aim of the study is to reproduce, in the simplified experimental configuration, the selective survival of minerals observed in the natural pseudotachylytes.

2. Material and methods

2.1 *Sample description (Mont Mary ultramylonite)*

The rock cylinders used in the experiment were cored from Mont Mary amphibolite-facies ultramylonites derived from coarse-grained sillimanite-garnet-biotite paragneiss (Fig. 1; Pennacchioni and Cesare, 1997). The fine-grained (1-5 μm) ultramylonite matrix consists of biotite + quartz ± ilmenite ± muscovite ± plagioclase. Rounded porphyroclasts of mm-sized plagioclase, sillimanite, and garnet are randomly scattered throughout the matrix (Pennacchioni et al., 2001). The ultramylonite displays fine, compositional banding defined by quartz ribbons and elongated plagioclase domains. The quartz ribbons range from monocrystalline to, more commonly, finely recrystallised aggregates (grain size ranging from 35 μm to 1 μm: Papa et al., 2020). Plagioclase (An_{35}) occurs as elongate aggregates of recrystallised (grain size < 5 μm) and rounded/elliptical porphyroclasts (up to mm-sized: Pennacchioni and Cesare, 1997). Sillimanite occurs as abundant rhomboid- to rectangular-shaped “mineral-fish” up to few hundred of μm in length (Pennacchioni et al., 2001). Garnet (Alm_{80}) occurs as mm-sized, rounded porphyroclasts. Garnet is commonly fractured and some cataclastic aggregates are deformed into elongate trails along the mylonitic foliation. Rare euhedral garnet (< 100 μm in size) is present in the ultramylonite matrix.

In the natural pseudotachylytes, survivor clasts are mostly quartz and sillimanite, and minor plagioclase. Sillimanite clasts are prismatic and apparently unaffected by fracturing, while quartz and plagioclase are locally surrounded by a cloud of fine-grained fragments (see Papa et al., 2018 supplementary figures). Garnet occurs as rare, small angular clasts.

'insert Figure 1 here'

2.2 *X-Ray Powder Diffraction*

The modal mineral amounts of the ultramylonite used in the experiment were determined by X-Ray Powder Diffraction (XRPD; Table 1). XRPD measurements were performed using a Philips X’Pert Pro MPD diffractometer equipped with a long-fine-focus cobalt anode tube working at 40 kV – 40 mA and a 240 mm goniometer radius that operates in the θ/θ geometry. Samples were prepared using the back-loading procedure in order to reduce preferred orientations of crystallites. Mineralogical species were identified using PANalytical High Score Plus v.4.8.0 (Malvern Panalytical Ltd, Malvern, UK). The fundamental parameters approach (Cheary et al., 2004) as implemented in Profex-BGMN v.4.1.0 (Doebelin and Kleeberg, 2015) was used in the Rietveld refinements.

2.3 *Rotary shear experiments*

The friction experiment was performed at atmospheric pressure and room humidity with the rotary machine SHIVA (Slow to High Velocity Apparatus: Di Toro et al., 2010) installed at the HPHT laboratory of the Istituto Nazionale di Geofisica e Vulcanologia in Rome (Italy). The experimental samples consisted of hollow cylinders (30/50 mm internal/external diameter) of the Mont Mary ultramylonites, cored parallel to the foliation. This core orientation allows full exposure of the ultramylonite compositional layering on the slip surface. Samples were jacketed in an aluminium ring and embedded in epoxy as described in Nielsen et al. (2012). Experimental conditions were: (i) 3 m/s target slip velocity; (ii) 40 m/s^2 slip acceleration and deceleration; (iii) 50 cm displacement (i.e. corresponding to the average fault slip associated to a Mw 6-7 earthquake; e.g. Scholz, 2019); and (iv) 20 MPa constant normal stress. Values of normal stress σ_n, equivalent displacement δ, equivalent slip velocity V, and shear stress τ were acquired during the experiments at a frequency of 12.5 kHz.

2.4 *Scanning Electron Microscopy and chemical maps*

Thin sections, cut perpendicular to the cylinder radius and to the slipping zone, were investigated with the Field Emission Scanning Electron Microscope (FE-SEM) MERLIN II ZEISS, equipped with both Energy Dispersive and Wavelength Dispersive spectrometers (ED/WD), at the CERTEMA multidisciplinary laboratory (Cinigiano, Italy). A cumulative area of 1.35 mm^2 of the experimental pseudotachylyte was mapped by high-resolution, back-scattered-electron (SEM-BSE) imaging. In the SEM-BSE images, plagioclase, quartz, and sillimanite clasts are difficult to distinguish from each other. Consequently, for mineral identification and clast size distribution studies, 10 randomly selected areas were analysed to produce Si, Al, Na, and Fe element maps. Maps and point chemical analyses were obtained combining ED/WD (equipped with five analysing crystals) spectrometry. The distribution of analyses between ED and WD spectrometers is consistent with both interfering peaks and synchronous measurement. The operative conditions and standardasing procedures were selected to minimise alkali loss and optimise the detection limits also in narrowing beam conditions. Analytical conditions were 15 kV accelerating voltage, 2 nA beam current, and 10 s peak and total background counting times. All maps have a rectangular grid of 2048x1536 pixels: low-magnification (LM) maps were taken at 8.5 pixels/μm and high-magnification (HM) maps at about 30-50 pixels/μm (Table 2).

2.5 *Image analysis*

Image SXM software was used for image analysis (https://www.liverpool.ac.uk/~sdb/ImageSXM/). The element maps were pre-processed by median filtering and thresholding. The same threshold values were used for the different maps of the same element. The resulting bitmaps were post-processed with the Erode and Dilate built-in functions to remove noise without modifying the grain shapes (Keulen et al., 2007; Heilbronner and Barrett, 2014). Only for the maps taken at the highest magnification, the boundaries of plagioclase and sillimanite clasts were traced manually. The clast size is expressed as diameter of the equivalent-area circle. Clast size distributions (CSDs) are plotted in a log-log plot of the cumulative frequency against the equivalent diameter for each mineral separately. The so-called two-dimensional fractal dimension D_{2D} is the slope of the best fit straight line of the distribution in the log-log plot, in the range in which the coefficient of correlation R^2 is greater than 0.99 (e.g. Montheil et al., 2020).

3. Results

3.1 *Mechanical data*

The evolution of the friction coefficient μ (= τ/σ_n), equivalent slip velocity, and normal stress σ_n as a function of slip and time during the experiment is presented in Figure 2. During frictional sliding, σ_n has small (± 5%) periodical oscillations with respect to the imposed target value of 20 MPa (Fig. 2B). At slip initiation, the value of μ increases up to a peak value of ~ 0.8 (Fig. 2B), corresponding to a shear stress (τ of ~ 16 MPa). Once the peak μ is overcome, the μ drops in ~ 10 cm of slip to a residual value of ~ 0.2 (τ ~ 4 MPa). During this frictional strength decay, the target velocity of ~3 m/s is achieved (Fig. 2A), and slip continues with a rather constant μ ~ 0.2 until slip deceleration takes place. Upon deceleration, μ increases toward the final value of ~ 0.35. The total displacement and slip duration are ~ 0.44 m and ~ 215 ms, respectively. The simulated slip pulse mimics the deformation conditions occurring in natural fault patches during moderate to large in magnitude earthquakes (Mw ≥ 6.0).

'insert Figure 2 here'

3.2 *Microstructures and analysis of clasts*

3.2.1 *Microstructures of experimental pseudotachylyte*

After the experiment, a continuous 150-200 μm-thick layer of quenched frictional melt (the experimental pseudotachylyte) decorates the slip surface (Fig. 3B). The pseudotachylyte contains abundant host-rock clasts set in a locally porous, but homogeneous matrix (Fig. 4A). The clasts are mostly monomineralic and consist of quartz, sillimanite, plagioclase, and garnet in a decreasing order of abundance (Fig. 5). No phyllosilicate survived as clasts. Ilmenite, present in the host rock as micrometric acicular crystals, is preserved within the pseudotachylyte only close to the wall-rock contact (Fig. 3B).

Clasts of quartz, sillimanite, and plagioclase are rarely larger than 30 μm and are homogeneously distributed across the pseudotachylyte. Garnet clasts cluster where the pseudotachylyte cuts the host-rock garnet (Fig. 4E). Large (max 35 μm) garnet clasts are commonly embedded in a lighter-coloured matrix (Fig. 4A) and locally associated with trails of smaller clasts stretched subparallel to the pseudotachylyte boundary (Fig. 4B). Except for these localised occurrences, the pseudotachylyte is devoid of garnet clasts. The host-rock garnet at the immediate contact with the pseudotachylyte, originally of several millimeters in size, is reduced to clasts down to the sub-micrometric size (Fig. 4C, 4D) with the smallest fragments (of nanometric dimensions) similar in composition to the host-rock garnet except for an apparent depletion in Fe and enrichment in Mg (Fig. S1). The pseudotachylyte matrix is homogeneous in SEM-BSE images, and contains abundant tiny (few hundreds of nanometers in size) microlites whose composition is enriched in Mg, Fe, and Al with respect to the matrix (Fig. S2). The small grain size of these microlites did not allow a more proper quantitative chemical analysis.

'insert Figure 3 and 4 here'

3.2.2 *Modal mineralogy*

In Figure 5 the volume percentages of quartz, plagioclase, sillimanite, and garnet in the ultramylonite (determined by X-Ray Powder Diffraction; Table 1) and the areal percentages of clasts in the pseudotachylyte (determined from image analysis of element maps; Fig. 6, 7; Table 2) are compared. In the host rock, quartz is the most abundant mineral (46.4 %), followed by plagioclase (11.9 %), sillimanite (7.7 %), and garnet (3.5 %).

'insert Table 1 here'

The measured areal percentage of clasts in element maps is in the range between 22 and 35 % (average 28 %) and does not vary systematically with increasing image magnification (Table 2). Quartz is the most abundant clast, followed by sillimanite, plagioclase, and garnet. The maps taken at approximately the same magnification show consistent results (Table 2): all the maps, regardless of the location and magnification, contain quartz (always by far the most abundant), sillimanite, and plagioclase clasts, but only two out of ten contain garnet clasts and none was detected in the HM maps. The abundance of plagioclase and sillimanite measured in HM maps is the same within error, while sillimanite is significantly more abundant than plagioclase in the LM maps.

'insert Figure 5, 6, 7 and Table 2 here'

3.2.3 *Clast size distributions*

Cumulative CSDs of individual minerals were measured in LM maps for plagioclase, sillimanite, and quartz (Fig. 8). CSDs for each mineral are substantially different. Quartz and plagioclase CSDs show a power-law distribution only for the larger clast sizes (right-hand side of the log-log distribution) while for grain sizes below a few μm they show a significant "left-hand fall-off" and no power-law distribution fit. For plagioclase, a linear fit of the log-log distribution is possible between approximately 0.6 and 5 μm, while at larger grain sizes the curve is steeper, indicating the presence of few coarse clasts. The D_{2D}-values are 1.2 for plagioclase, 1.9 for sillimanite, and 2.5 for quartz (Fig. 8). However, the CSDs show a power-law distribution over a size range of approximately one order of magnitude (plagioclase and quartz) or even less (sillimanite). The total number of clasts of plagioclase and sillimanite is similar, but small clasts of plagioclase are more abundant than those of sillimanite. This is particularly evident in HM maps, where the smallest clasts (e.g. < 1 μm) can be detected more accurately (Fig. 8D).

'insert Figure 8 here'

4. Discussion

4.1 *Melting temperature of minerals*

Frictional melts are generally assumed to form under non-equilibrium conditions and minerals to melt at their individual melting temperature (Spray, 2010), although quasi-equilibrium melting of quartzite during high-speed experiments with large imposed slip has been proposed (Lee et al., 2017). However, under non-equilibrium conditions, the melting temperatures of single minerals are not well known, since most petrological experiments are carried out at equilibrium and minerals either melt incongruently or react to form high-temperature assemblages before melting.

Phyllosilicates are generally considered to have the lowest melting point temperature, generally lower than ~ 700-900 °C (Spray, 2010; Hung et al., 2019). Plagioclase (An_{35}), at equilibrium, begins to melt incongruently at 1200 °C and reaches the liquidus at 1400 °C (Bowen, 1913). Quartz (α) transforms to β-quartz at 573 °C, and enters the stability field of tridymite and cristobalite before melting at 1715 °C (generally regarded as the melting temperature of quartz; Tuttle and Bowen, 1958). However, based on experimental observations, it has also been proposed that, during frictional slip, quartz could melt at temperatures of 1350 to 1500 °C (Lee et al., 2017). Sillimanite breaks down to mullite and a silica phase above 1300 °C (Schneider and Komarneni, 2006). However, this transformation is sluggish and sillimanite can survive metastably up to 1660 °C (Schneider and Majdic, 1981). In our experiment, there is no evidence of sillimanite breakdown to mullite. In the Al_2O_3-SiO_2 phase diagram, pure mullite melts congruently above 1800 °C, while a composition corresponding to sillimanite starts incongruent melting at 1600 °C and reaches the liquidus at 1850 °C (Aramaki and Roy, 1962). Therefore, the sillimanite melting temperature, despite not being precisely established, is apparently high (perhaps higher than that of quartz). The same issue applies to almandine-rich garnet that, under equilibrium at low pressures, decomposes to Fe-cordierite + fayalite + hercynite before melting (Hsu, 1968; Keesmann et al., 1971). It has been reported that congruent melting of spessartine occurs at ~ 1200 °C at atmospheric pressure (Snow, 1943), and the same temperature is reported by Spray (2010) for the melting/breakdown of almandine. However, observation of nanometric garnet clasts with a chemical composition slightly different than the adjacent host-rock garnet, suggests that garnet may be melting incongruently during the experiment.

Despite the large uncertainties described above, the following single-mineral melting temperatures can be reasonably assumed: (i) < 700-900 °C for phyllosilicates; (ii) ~ 1200 °C for garnet; (iii) ~ 1200-1400 °C for plagioclase (An_{35}); and (iv) > 1700 °C for quartz and sillimanite (Table S1). In this assumption, deliberately we did not take into account any additional processes that may lower melting temperatures during high-speed frictional slip (Lee et al., 2017), of which very little is known.

4.2 *Temperature evolution and thermal shock*

Theoretical and experimental studies on seismic slip indicate that flash heating can abruptly raise the temperature at the asperity contacts (few tens of micrometers in diameter) up to the melting point after few tens of micro- to milli-seconds (flash temperatures, e.g., Goldsby and Tullis, 2011; Rempel and Weaver, 2008). As an example, Violay et al. (2014) reported the formation of solidified melt microstructures in microgabbro sheared up to a peak velocity of 0.23 m/s after only 5 mm of slip corresponding to ~ 0.20 ms of slip duration. In calcite-bearing rocks, Spagnuolo et al. (2015) documented emission of CO_2 and formation of patches made of amorphous carbon on the sample surface after only 1.5 mm of slip (i.e. < 10 ms of slip duration). This microstructural evidence suggested that the de-carbonation reaction, expected to occur at about 900 °C (Rodriguez-Navarro et al., 2009), was activated, at least within the calcite lattice (i.e., dislocation avalanche model: Spagnuolo et al., 2015). Unfortunately, the detection of flash temperatures is a technical challenge. For instance, thermocouples can measure temperature directly on the fault surface (if are not cut during frictional sliding) but have a large inertia (0.1 s) compared to the timescale of flash heating, and poor spatial resolution (several mm). Very recently, Aretusini et al. (2021) estimated the experimental fault temperatures every ms over a spatial resolution of ~ 40 μm by using a two-color optical fiber pyrometer to measure the infrared radiation emitted from the sliding surface. In these experiments performed on Carrara marble at loading conditions similar to those imposed in experiments S1771, the temperature climbed up to ~ 1000 °C after few milliseconds. Unfortunately, data for silicate rocks are not available yet, though there is no reason to exclude that such high temperatures can be achieved after few mm of simulated seismic slip in cohesive rocks (see Violay et al., 2014). Collectively these studies indicate that frictional heating can raise easily the temperature to above melting after a few ms of seismic slip.

In experiment S1771, the frictional drop from the initial peak to the minimum occurs in about 70 ms (Fig. 2). This first friction drop in rotary shear experiments is generally referred to flash heating and weakening (Rice, 2006; Beeler et al., 2008). Initial friction drop is usually followed, at least in experiments performed at low normal stress (e.g., < 20 MPa), by a re-strengthening stage associated to the formation of highly viscous and discontinuous melt patches in the slipping zone (Hirose and Shimamoto, 2005; Hung et al., 2019), before bulk melting and steady-state conditions are achieved (Nielsen et al., 2008; 2010). In experiment S1771 we observe only one initial phase of weakening, completed after ~ 70 ms, after which the "friction coefficient" remains low with small oscillations (0.15-0.25); re-strengthening is only observed when the slip velocity decelerates at the end of the experiment (Fig. 2). This experimental evidence suggests that, because of the relatively high normal stress (20 MPa), high slip velocity and acceleration (3 m/s and 40 m/s^2, respectively) and the abundance of low-melting point minerals (phyllosilicates), a continuous layer of melt forms in less than 100 ms. This implies a temperature increase of 700-900 °C in less than 100 ms. At the end of the experiment (after 200 ms), the temperature necessary to melt, at least partially, high-melting minerals like sillimanite and quartz is certainly achieved: we infer that temperature increased up to 1500 °C in about 200 ms or less.

Such sudden temperature increase and severe thermal gradients induced in a solid result in thermal stresses due to differential thermal expansion (Kingery, 1955). In a spherical body, compressive stresses develop at the surface and tensile stresses in the core (Geller, 1972). In more irregularly-shaped bodies, like angular clasts, the highest tensile stress buildup at the roots of sharp corners of the surface (Roy et al., 2012). For diabase and metasedimentary rock compositions, Roy et al. (2012) calculated maximum instantaneous tensile stresses of the order of 40-50 MPa for an initial difference of 250 °C between clast and melt. During our experiment the thermal gradients are much larger, and therefore tensile stresses within clasts of the experimental pseudotachylyte certainly reached the mineral tensile strength (hardly much higher than a few tens of MPa: e.g. Zhang, 2002), although this strength increases significantly when the particle size approaches the comminution limit. Thus, thermal shock is an important mechanism of comminution during frictional melting, increasing the surface area of minerals and facilitating their melting. This process is also known as marginal decrepitation (Sibson, 1975), although originally explained by fluid expansion rather than by thermal stresses. The intensity of thermal stresses, and therefore the resistance to thermal shock, depends on the mineral thermomechanical properties (e.g., Lu and Fleck, 1997). Papa et al. (2018) showed that garnet has the lowest thermal-shock resistance, followed by plagioclase, quartz, and sillimanite (Table S1).

4.3 *Selective preservation of minerals*

The observed frictional melting susceptibility of host-rock minerals in the experimental sample corresponds to that observed in nature (Papa et al., 2018): (i) quartz and sillimanite are the least susceptible to melting and survive as abundant clasts; (ii) plagioclase is more prone to melting but still survives as abundant small clasts; (iii) garnet strongly comminutes and melts extensively; and (iv) phyllosilicates are not preserved as clasts. Actually, during our high-velocity rotary shear experiment, minerals with the lowest thermal shock strength (garnet) that are initially preferentially finely pulverized can be expelled from the slip surface and this may also explain the relative scarcity of garnet between clasts in the artificial pseudotachylyte. However, in natural seismic faults, initially pulverized materials produced by wear and thermal shock could not leave the fault- and the injection-veins and are entrapped as clasts in the melt (pseudotachylyte). The strong correspondence between the selective disappearance of the different minerals in the natural and artificial pseudotachylyte formed in the Mont Mary ultramylonite is taken as the evidence that melting actually played the main role in role obliterating selectively the most comminuted fine-grained clasts. In any case, even assuming that powder expulsion is the cause for the dramatic garnet decrease between the clasts of the artificial pseudotachylyte, this would imply all the same that preferential thermal shock comminution of garnet did occur.

During the experiment, all minerals experienced some degree of melting (Fig. 5). This implies that the high melting temperatures of quartz and sillimanite were reached. However, because of the short duration of the heat pulse (less than 250 ms) and low thermal conductivity of minerals, coarse clasts escaped complete melting (Ray, 1999). This highlights the strong influence of selective comminution in melting susceptibilities of minerals. The measured abundance of plagioclase clasts depends on the scale of the observation, being higher in HM-maps than in LM-maps (even when they are taken from the same area). This is due to the larger population of small clasts with respect to the other minerals, as also shown by CSDs (Fig. 8D). In fact, small clasts (e.g., < 1-2 μm) might be largely overlooked in LM maps (Fig. 7F), while they are detected in HM maps. This result is consistent with plagioclase experiencing a higher degree of melting due to lower melting temperature than sillimanite and quartz. However, garnet, despite having a melting temperature similar to plagioclase, does not show the same widespread occurrence.

4.4 *Disappearance of garnet in pseudotachylyte*

Several authors reported the scarcity of garnet clasts in pseudotachylytes (e.g. Camacho et al., 1995; Austrheim et al., 1996; Altenberger et al., 2013; Pittarello et al., 2012) and the extreme comminution of garnet adjacent to pseudotachylyte veins (Austrheim et al., 2017; Papa et al., 2018; Hawemann et al., 2019b; Petley-Ragan et al., 2019). Garnet comminution has been referred to seismic loading (Trepmann and Stöckhert, 2002; Austrheim et al., 2017), dynamic propagation of seismic rupture (Petley-Ragan et al., 2019), and thermal shock (Papa et al., 2018). Because of the chosen sample assemblage (in the experimental fault the two pre-cut rock cylinders are in contact along a cohesionless slip surface), in the rotary shear experiments the effects of the dynamic rupture may be considered negligible. Moreover, given the high imposed acceleration and the large frictional power (~ 20 MW/m^2 or the product of shear stress per slip rate, Di Toro et al., 2011) dissipated in the experiment, the temperature gradients away from the slipping zone are negligible as well (see Nielsen et al. 2008 and 2010 for discussion). Notably, (i) intense wall-rock garnet fragmentation is not observed, except at the very host rock/pseudotachylyte interface (Fig. 4C), (ii) within the pseudotachylyte, garnet is scarce and clustered in distribution (which suggests that the preserved clasts were readily molten) and, (iii) garnet clasts are commonly located close to the border of the vein (Fig. 4E) and surrounded by a lighter-coloured matrix (Fig. 4A) (likely a Fe-enriched melt derived by *in-situ* melting of garnet). All these features suggest that garnet clasts were detached from the host rock and dispersed in the melt at a “late stage” of the experiment. A few hundreds of milliseconds were enough to melt garnet in the vein interior, where the highest temperatures were attained and maintained for a longer period of time (e.g., Di Toro and

Pennacchioni, 2004; Nielsen et al., 2008). A similar behaviour is inferred for ilmenite that has a melting temperature of ~ 1470 °C (Spray, 2010). It is commonly observed that ilmenite clasts are only preserved close to the vein border (Fig. 3B). Ilmenite occurs in the host rock as few-micrometer-long acicular crystals with a large surface/volume ratio and therefore melts very fast if its melting temperature is reached. These conditions were likely achieved in the vein centre and not at the border, consistently with thermal modelling of pseudotachylytes (Nielsen et al., 2008). On the other hand, garnet is present in the rock as porphyroclasts as large as few millimetres and must undergo extreme comminution in order to melt extensively during the short time of the experiment However, garnet has a lower efficiency of comminution (Tromans, 2008) and a higher fracture toughness (Tromans and Meech, 2004) with respect to plagioclase (Table S1): therefore, the preferential comminution and associated melting of garnet is better explained by its low thermal shock resistance (Papa et al., 2018). The general scarcity of survival clasts can also explain the rarity of garnet microlites in many occurrences of deep seated pseudotachylytes, where garnet should be stable. Although microlites do not necessarily grow around a clast of the same mineral (e.g. Sarkar and Chattopadhyay, 2020); garnet microlites (especially the so-called cauliflower garnet) commonly show relict clast nuclei at their cores (Altenberger et al., 2013; Pittarello et al., 2015).

4.5 *Clast size distribution in frictional melts*

The post-melting CSD is strongly dependent on the mineralogy of clasts (Fig. 8). The initial, pre-melting size distribution is also influenced by the original mineral grain size in the host ultramylonite. Some minerals (quartz, phyllosilicates, and locally plagioclase) were present as aggregates of small (few μm in size) recrystallised grains in the ultramylonite. Since the fracture toughness for grain boundary cracking is less than that for intragranular cracking (Tromans and Meech, 2004), these minerals will tend to disaggregate along pre-existent grain boundaries and thus their initial size distribution will include abundant small clasts. The mineral proportions of these fine-grained clasts surviving melting vary depending on whether the minerals have high- or low-melting points. Minerals like garnet and sillimanite, present as larger single-crystal porphyroclasts in the host ultramylonite, undergoes comminution by intragranular cracking. It has also been suggested that additional ultrafine grains can derive from thermal cracking after the frictional melt covers the entire slip surface (Hung et al., 2019).

The pre-melting particle-size distribution resulting from comminution is ideally characterised by a power-law distribution (e.g., Sammis and Biegel, 1989), although Phillips and Williams (2021) have recently proposed that log-normal distributions provide a better description in most cases. After melting, this distribution is modified and the CSDs generally observed in pseudotachylytes are consistent with our experimental observations (Fig. 8; Shimamoto and Nagahama, 1992; Tsutsumi, 1999; Ray, 1999; Behera et al., 2017; Hung et al., 2019; Sarkar et al., 2020). Assuming a uniform rim melting of clasts, the population of large clasts basically retains the pre-melting size distribution if the degree of melting is not too high, while the finer size fraction is significantly modified to smaller D-values than in the pre-melting distribution (Ray, 2004). The post-melting D-value is thus a minimum estimate of the pre-melting D-value: the higher the degree of melting the more it will diverge from it. Assuming that the D_{2D} for quartz (≥ 2.5) measured over a grain size range of only one order in magnitude (Fig. 4) can be extended over larger grain sizes, the D_{2D} would be consistent with that reported by Muto et al. (2015) in pulverised fault rocks in close proximity to fault cores (~ 2.7). These authors refer this high D-value to seismic rupture propagation. Instead, our results suggest that similar D-values are obtained by comminution and melting during frictional seismic slip, even in the absence of a significant effect of rupture propagation as is the case of our experimental configuration. At least, this conclusion is valid for the slip distances (0.5 m) presented in this study, which are typical of moderate- to large-magnitude earthquakes (Scholz, 2019). In the case of shorter seismic slip episodes (= small-magnitude earthquakes), the volume of melt production would be smaller, the time of interaction between clasts and melt shorter, and the CSD possibly different from the one found in this study.

4.6 *Seismic rupture propagation vs seismic slip*

Field-based, experimental and theoretical studies have shown that fracturing, associated with seismic faulting, potentially results from different mechanisms including the stages of dynamic fracture propagation and subsequent frictional fault slip (e.g., Ben Zion and Shi, 2005). Some authors reported in-situ fracturing, in pseudotachylyte-bearing rocks, relatively distant from the fault and therefore not ascribable to thermomechanical processes associated with seismic frictional fault slip (Austrheim et al., 2017; Petley-Ragan et al., 2019). Wall rock pulverization during dynamic rupture is also observed in ultra-high pressure experiments (Incel et al., 2019).

Our experiment, performed on surfaces that were pre-cut, do not reproduce the stage of earthquake rupture propagation and the thermomechanical process only includes the stage of frictional slip and melting. Therefore, we can evaluate the result of seismic slip and related transient, thermal effects, separately from the dynamic rupture propagation effect. We observe that no off-fault damage is induced in the host rock during seismic slip, different to what is observed in nature (Di Toro et al., 2005). However, our experiment successfully reproduced the microstructure and the relative mineral behaviour of natural pseudotachylytes, suggesting that, for $M_w \geq 6$ earthquakes, dissipative processes associated to frictional sliding and heating have a major control on clast survival.

5. **Conclusions**

Our results show that the selective preservation of host-rock clasts observed in natural pseudotachylytes can be reproduced in frictional melts produced in a rotary shear machine. The microstructural investigation of the experimental pseudotachylyte confirms that the minerals preferentially preserved as clasts are those with high individual melting temperature and high thermal shock resistance. This explains the common disappearance of garnet clasts in natural pseudotachylytes. At ambient conditions at which garnet should be stable (e.g., in the middle to lower continental crust), the reported scarcity or absence of garnet microlites can be explained by the absence of survival clasts that serve as nucleation seeds for microlite growth (Pittarello et al., 2015).

In our experiments, slip localized on the pre-cut surfaces. This experimental configuration does not reproduce the stage of dynamic rupture propagation and associated large stress perturbation that causes severe off-fault damage in natural pseudotachylytes (Di Toro et al., 2005). However, the experiment reproduces accurately the mechanical behaviour of minerals in natural pseudotachylytes. We conclude that, for Mw ≥ 6 earthquakes, (i) frictional slip and heating of the slip zone and (ii) thermomechanical properties of individual minerals, rather than fault rupture processes, have a major control on mineral comminution and clast survival in seismic melts.

Acknowledgements

This work was supported by: University of Padova BIRD175145/17 (G.P.), European Research Council CoG project 614750 NOFEAR (G.D.T. and E.S.), and NSERC Discovery Grant 2018-06023 (A.Cam.). The authors thank Leonardo Tauro (University of Padova) for thin section preparation.

The authors acknowledge two anonymous reviewers and the Editor Fabrizio Agosta for their constructive comments.

CRediT author statement

Simone Papa: Conceptualization, Investigation (experiments), Writing - Original Draft; **Elena Spagnuolo:** Conceptualization, Investigation (experiments), Writing - Review & Editing; **Giulio Di Toro:** Conceptualization, Writing - Review & Editing, Funding acquisition; **Andrea Cavallo:** Investigation (SEM), Writing - Review & Editing; **Marco Favero:** Investigation (XRPD), Writing - Review & Editing; **Alfredo Camacho:** Writing - Review & Editing, Funding acquisition; **Giorgio Pennacchioni:** Conceptualization, Writing - Review & Editing, Supervision, Funding acquisition.

References

Altenberger, U., Prosser, G., Grande, A., Günter, C., & Langone, A. (2013). A seismogenic zone in the deep crust indicated by pseudotachylytes and ultramylonites in granulite-facies rocks of Calabria (Southern Italy). *Contributions to Mineralogy and Petrology*, *166*(4), 975–994. https://doi.org/10.1007/s00410-013-0904-3

Aramaki, S., and Roy, R. (1962). Revised Phase Diagram for the System Al2O3—SiO2. *Journal of the American Ceramic Society*, *45*(5), 229–242. https://doi.org/10.1111/j.1151-2916.1962.tb11133.x

Austrheim, H., Dunkel, K. G., Plümper, O., Ildefonse, B., Liu, Y., and Jamtveit, B. (2017). Fragmentation of wall rock garnets during deep crustal earthquakes. *Science Advances*, *3*(2), 1–8. https://doi.org/10.1126/sciadv.1602067

Austrheim, H., Erambert, M., and Boundy, T. M. (1996). Garnets recording deep crustal earthquakes. *Earth and Planetary Science Letters*, *139*(1–2), 223–238. https://doi.org/10.1016/0012-821x(95)00232-2

Behera, B. M., Thirukumaran, V., Soni, A., Mishra, P. K., and Biswal, T. K. (2017). Size distribution and roundness of clasts within pseudotachylytes of the gangavalli shear zone, Salem, Tamil Nadu: An insight into its origin and tectonic significance. *Journal of Earth System Science*, *126*(4). https://doi.org/10.1007/s12040-017-0827-x

Ben-Zion, Y., and Shi, Z. (2005). Dynamic rupture on a material interface with spontaneous generation of plastic strain in the bulk. *Earth and Planetary Science Letters*, *236*(1–2), 486–496. https://doi.org/10.1016/j.epsl.2005.03.025

Bowen, N. L. (1913). The melting phenomena of the plagioclase feldspar. *American Journal of Science*, *35*, 577-599. DOI: https://doi.org/10.2475/ajs.s4-35.210.577.

Camacho, A., Vernon, R. H., and Fitz Gerald, J. D. (1995). Large volumes of anhydrous pseudotachylyte in the Woodroffe Thrust, eastern Musgrave Ranges, Australia. *Journal of Structural Geology*, *17*(3), 371–383. https://doi.org/10.1016/0191-8141(94)00069-C

Cheary, R. W., Coelho, A. A., and Cline, J. P. (2004). Fundamental parameters line profile fitting in laboratory diffractometers. *Journal of Research of the National Institute of Standards and Technology*, *109*(1), 1–25. doi: 10.6028/jres.109.002.

Di Toro, G., and Pennacchioni, G. (2004). Superheated friction-induced melts in zoned pseudotachylytes within the Adamello tonalites (Italian Southern Alps). *Journal of Structural Geology*, *26*(10), 1783–1801. https://doi.org/10.1016/j.jsg.2004.03.001

Di Toro, G., Nielsen, S., and Pennacchioni, G. (2005). Earthquake rupture dynamics frozen in exhumed ancient faults. *Nature*, *436*(7053), 1009–1012. https://doi.org/10.1038/nature03910

Di Toro, G., Niemeijer, A., Tripoli, A., Nielsen, S., Di Felice, F., Scarlato, P., Spada, G., Alessandroni, R., Romeo, G., Di Stefano, G., Smith, S., Spagnuolo, E., and Mariano, S. (2010). From field geology to earthquake simulation: A new state-of-The-art tool to investigate rock friction during the seismic cycle (SHIVA). *Rendiconti Lincei*, *21*(SUPPL. 1), 95–114.

https://doi.org/10.1007/s12210-010-0097-x

Di Toro, G., Han, R., Hirose, T., De Paola, N., Nielsen, S., Mizoguchi, K., Ferri, F., Cocco, M., and Shimamoto, T. (2011). Fault lubrication during earthquakes. *Nature*, *471*(7339), 494–499. https://doi.org/10.1038/nature09838

Doebelin, N., and Kleeberg, R. (2015). Profex: A graphical user interface for the Rietveld refinement program BGMN. *Journal of Applied Crystallography*, *48*, 1573–1580. doi: 10.1107/S1600576715014685.

Geller, L. B. (1972). Thermal stresses in spheres-A basis for studying the grinding of preheated rocks. *International Journal of Rock Mechanics and Mining Sciences And*, *9*(2), 213–240. https://doi.org/10.1016/0148-9062(72)90024-1

Hawemann, F., Mancktelow, N., Wex, S., Pennacchioni, G., and Camacho, A. (2019). Fracturing and crystal plastic behaviour of garnet under seismic stress in the dry lower continental crust (Musgrave Ranges, Central Australia). *Solid Earth*, *10*(5), 1635–1649. https://doi.org/10.5194/se-10-1635-2019

Heaton, T. H. (1990). Evidence for and implications of self-healing pulses of slip in earthquake rupture. *Physics of the Earth and Planetary Interiors*, *64*(1), 1–20. https://doi.org/10.1016/0031-9201(90)90002-F

Heilbronner, R., Barrett, S. (2014). Image Analysis in Earth Sciences: Microstructures and Textures of Earth Materials. *Springer Science and Business Media*

Hsu, L. C. (1968). Selected phase relationships in the system Al-Mn-Fe-Si-O-H: A model for garnet equilibria. *Journal of Petrology*, *9*(1), 40–83. https://doi.org/10.1093/petrology/9.1.40

Incel, S., Schubnel, A., Renner, J., John, T., Labrousse, L., Hilairet, N., Freeman, H., Wang, Y., Renard, F., and Jamtveit, B. (2019). Experimental evidence for wall-rock pulverization during dynamic rupture at ultra-high pressure conditions. *Earth and Planetary Science Letters*, *528*, 115832. https://doi.org/10.1016/j.epsl.2019.115832

Keesmann, I., Matthes, S., Schreyer, W., and Seifert, F. (1971). Stability of almandine in the system

FeO-(Fe2O3)-Al2O3-SiO2-(H2O) at elevated pressures. *Contributions to Mineralogy and Petrology*, *31*(2), 132–144. https://doi.org/10.1007/BF00373456

Keulen, N., Heilbronner, R., Stünitz, H., Boullier, A. M., and Ito, H. (2007). Grain size distributions of fault rocks: A comparison between experimentally and naturally deformed granitoids. *Journal of Structural Geology*, *29*(8), 1282–1300. https://doi.org/10.1016/j.jsg.2007.04.003

Lee, S. K., Han, R., Kim, E. J., Jeong, G. Y., Khim, H., and Hirose, T. (2017). Quasi-equilibrium melting of quartzite upon extreme friction. *Nature Geoscience, 10*, 436-442. DOI: 10.1038/NGEO2951

Lu, T. J., and Fleck, N. A. (1998). The thermal shock resistance of solids. *Acta Materialia*, *46*(13), 4755–4768. https://doi.org/10.1016/S1359-6454(98)00127-X

Maddock, R. H. (1974). Melt origin of fault-generated pseudotachylytes. *Geology*, *11*, 105–108. https://doi.org/10.1130/0091-7613(1983)11<105

Maddock, R. H. (1992). Effects of lithology, cataclasis and melting on the composition of fault-generated pseudotachylytes in Lewisian gneiss, Scotland. *Tectonophysics*, *204*(3–4), 261–278. https://doi.org/10.1016/0040-1951(92)90311-S

Magloughlin, J. F. (1989). The nature and significance of pseudotachylite from the Nason terrane, North Cascade Mountains, Washington. *Journal of Structural Geology*, *11*(7), 907–917. https://doi.org/10.1016/0191-8141(89)90107-7

Montheil, L., Toy, V. G., Scott, J. M., Mitchell, T. M. and Dobson, D. P. (2020). Impact of Coseismic Frictional Melting on Particle Size, Shape Distribution and Chemistry of Experimentally-Generated Pseudotachylite. *Frontiers in Earth* Sciences, 8, 596116. doi: 10.3389/feart.2020.596116

Muto, J., Nakatani, T., Nishikawa, O., and Nagahama, H. (2015). Fractal particle size distribution of pulverized fault rocks as a function of distance from the fault core. *Geophysical Research Letters*, *42*(10), 3811–3819. https://doi.org/10.1002/2015GL064026

Nielsen, S., Di Toro, G., Hirose, T., and Shimamoto, T. (2008). Frictional melt and seismic slip.

Journal of Geophysical Research: Solid Earth, *113*(1), 1–20. https://doi.org/10.1029/2007JB005122

Nielsen, S., Mosca, P., Giberti, G., Di Toro, G., Hirose, T., and Shimamoto, T. (2010). On the transient behavior of frictional melt during seismic slip. *Journal of Geophysical Research: Solid Earth*, *115*(10), 1–17. https://doi.org/10.1029/2009JB007020

Nielsen, S., Spagnuolo, E. and Violay, M. (2012) The ultimate sample preparation for rotary shear experiments. *Rapporti Tecnici INGV* 215, 1–16.

O'Hara, K. (1992). Major- and trace-element constraints on the petrogenesis of a fault-related pseudotachylyte, western Blue Ridge province, North Carolina. *Tectonophysics*, *204*(3–4), 279–288. https://doi.org/10.1016/0040-1951(92)90312-T

Okubo, K., Bhat, H. S., Rougier, E., Marty, S., Schubnel, A., Lei, Z., Knight, E. E., and Klinger, Y. (2019). Dynamics, Radiation, and Overall Energy Budget of Earthquake Rupture With Coseismic Off-Fault Damage. *Journal of Geophysical Research: Solid Earth*, *124*(11), 11771–11801. https://doi.org/10.1029/2019JB017304

Papa, S., Pennacchioni, G., Angel, R. J., and Faccenda, M. (2018). The fate of garnet during (deep-seated) coseismic frictional heating: The role of thermal shock. *Geology*, *46*(5). https://doi.org/10.1130/G40077.1

Papa, S., Pennacchioni, G., Menegon, L., and Thielmann, M. (2020). High-stress creep preceding coseismic rupturing in amphibolite-facies ultramylonites. *Earth and Planetary Science Letters*, *541*. https://doi.org/10.1016/j.epsl.2020.116260

Pennacchioni, G., and Cesare, B. (1997). Ductile-brittle transition in pre-Alpine amphibolite facies mylonites during evolution from water-present to water-deficient conditions (Mont Mary nappe, Italian Western Alps). *Journal of Metamorphic Geology*, *15*(6), 777–791. https://doi.org/10.1111/j.1525-1314.1997.00055.x

Pennacchioni, G., Di Toro, G., and Mancktelow, N. S. (2001). Strain-insensitive preferred orientation of porphyroclasts in Mont Mary mylonites. *Journal of Structural Geology*, *23*(8), 1281–1298. https://doi.org/10.1016/S0191-8141(00)00189-9

Petley-Ragan, A., Ben-Zion, Y., Austrheim, H., Ildefonse, B., Renard, F., and Jamtveit, B. (2019). Dynamic earthquake rupture in the lower crust. *Science Advances*, *5*(7). https://doi.org/10.1126/sciadv.aaw0913

Phillips, N. J., and Williams, R. T. (2021). To D or not to D? Re-evaluating particle-size distributions in natural and experimental fault rocks. *Earth and Planetary Science Letters*, *553*, 116635. https://doi.org/10.1016/j.epsl.2020.116635

Pittarello, L., Pennacchioni, G., and Di Toro, G. (2012). Amphibolite-facies pseudotachylytes in Premosello metagabbro and felsic mylonites (Ivrea Zone, Italy). *Tectonophysics*, *580*, 43–57. https://doi.org/10.1016/j.tecto.2012.08.001

Ray, S. K. (1999). Transformation of cataclastically deformed rocks to pseudotachylyte by pervasion of frictional melt: Inferences from clast-size analysis. *Tectonophysics*, *301*(3–4), 283–304. https://doi.org/10.1016/S0040-1951(98)00229-7

Ray, S. K. (2004). Melt - Clast interaction and power-law size distribution of clasts in pseudotachylytes. *Journal of Structural Geology*, *26*(10), 1831–1843. https://doi.org/10.1016/j.jsg.2004.02.009

Reches, Z., and Dewers, T. A. (2005). Gouge formation by dynamic pulverization during earthquake rupture. *Earth and Planetary Science Letters*, *235*(1–2), 361–374. https://doi.org/10.1016/j.epsl.2005.04.009

Roy, S. G., Johnson, S. E., Koons, P. O., and Jin, Z. (2012). Fractal analysis and thermal-elastic modeling of a subvolcanic magmatic breccia: The role of post-fragmentation partial melting and thermal fracture in clast size distributions. *Geochemistry, Geophysics, Geosystems*, *13*(5), 1–23. https://doi.org/10.1029/2011GC004018

Sammis, C. G., and Biegel, R. L. (1989). Fractals, Fault-Gouge, and Friction. *Pure and Applied Geophysics*, *131*, 255-271. https://doi.org/10.1007/BF00874490

Sarkar, A., Bhattacharjee, D., and Chattopadhyay, A. (2020). Size distribution of survivor clasts in pseudotachylyte and cataclasite: Implications for crushing and melting processes in seismic fault zones. *Journal of Earth System Science, 129*(1). https://doi.org/10.1007/s12040-020-01480-3

Schneider, H. and Majdic, A. (1981). Preliminary investigations on the kinetics of the high-temperature transformation of sillimanite to 3/2-mullite plus silica and comparison with the behaviour of andalusite and kyanite. *Sci. Ceram., 11*, 191–196.

Schneider, H., and Komarneni, S. (2006). Mullite. *John Wiley & Sons*.

Scholz, C. H. (2019). The mechanics of earthquakes and faulting. *Cambridge University Press*.

Shand, J. S. (1916). The pseudotachylyte of Parijs (Orange Free state), and its relation to trap-Shotten gneiss and flinty Crush-Rock. *Quarterly Journal of the Geological Society of London, 72*(1–4), 198–221. https://doi.org/10.1144/GSL.JGS.1916.072.01-04.12

Shimamoto, T., and Nagahama, H. (1992). An argument against the crush origin of pseudotachylytes based on the analysis of clast-size distribution. *Journal of Structural Geology*, *14*(8–9), 999–1006. https://doi.org/10.1016/0191-8141(92)90031-Q

Sibson, R. H. (1975). Generation of Pseudotachylyte by Ancient Seismic Faulting. *Geophysical Journal of the Royal Astronomical Society*, *43*(3), 775–794. https://doi.org/10.1111/j.1365-246X.1975.tb06195.x

Snow, R. B. (1943). Equilibrium relationships on the liquidus surface in part of the MnO-Al2O3-SiO2 system. *Journal of the American Ceramic Society*, *26*(1), 11–20. https://doi.org/10.1111/j.1151-2916.1943.tb15177.x

Spray, J. G. (1987). Artificial generation of pseudotachylyte using friction welding apparatus: simulation of melting on a fault plane. *Journal of Structural Geology*, *9*(1), 49–60. https://doi.org/10.1016/0191-8141(87)90043-5

Spray, J. G. (1995). Pseudotachylyte controversy: fact or friction? *Geology*, *23*(12), 1119–1122. https://doi.org/10.1130/0091-7613(1995)023<1119:PCFOF>2.3.CO;2

Spray, J. G. (1992). A physical basis for the frictional melting of some rock-forming minerals.

Tectonophysics, *204*(3–4), 205–221. https://doi.org/10.1016/0040-1951(92)90308-S

Spray, J. G. (2010). Frictional Melting Processes in Planetary Materials: From Hypervelocity Impact to Earthquakes. *Annual Review of Earth and Planetary Sciences*, *38*(1), 221–254. https://doi.org/10.1146/annurev.earth.031208.100045

Trepmann, C. A., and Stöckhert, B. (2002). Cataclastic deformation of garnet: A record of synseismic loading and postseismic creep. *Journal of Structural Geology*, *24*(11), 1845–1856. https://doi.org/10.1016/S0191-8141(02)00004-4

Tromans, D., and Meech, J. A. (2004). Fracture toughness and surface energies of covalent minerals: Theoretical estimates. *Minerals Engineering*, *17*(1), 1–15. https://doi.org/10.1016/j.mineng.2003.09.006

Tromans, D. (2008). Mineral comminution: Energy efficiency considerations. *Minerals Engineering*, *21*(8), 613–620. https://doi.org/10.1016/j.mineng.2007.12.003

Tsutsumi, A. (1999). Size distribution of clasts in experimentally produced pseudotachylytes. *Journal of Structural Geology*, *21*(3), 305–312. https://doi.org/10.1016/S0191-8141(98)00113-8

Tuttle, O.F., and Bowen, N.L. (1958). Origin of granite in the light of experimental studies in the system $NaAlSi_3O_8$-$KAlSi_3O_8$-SiO_2-H_2O. *The Geological Society of America Memoir, 74.*

Violay, M., Nielsen, S., Gibert, B., Spagnuolo, E., Cavallo, A., Azais, P., Vinciguerra, S., and Di Toro, G. (2014). Effect of water on the frictional behavior of cohesive rocks during earthquakes. *Geology*, *42*(1), 27–30. https://doi.org/10.1130/G34916.1

Wenk, H. R. (1978). Are pseudotachylites products of fracture or fusion? *Geology*, *6*(8), 507–511. https://doi.org/10.1130/0091-7613(1978)6<507:APPOFO>2.0.CO;2

Zhang, Z. X. (2002). An empirical relation between mode I fracture toughness and the tensile strength of rock. *International Journal of Rock Mechanics and Mining Sciences*, *39*(3), 401–406. https://doi.org/10.1016/S1365-1609(02)00032-1

Figure captions

Figure 1 A) Two hollow cilinders of Mont Mary ultramylonite cored perpendicular to the foliation. Black arrows indicate visible garnet crystals on the surface. B) Samples mounted on SHIVA, before the experiment. C) Samples after the experiment. The cut vertical surface of the sample on the right-hand-side shows the orientation of the thin sections studied in this paper. D) Thin section of Mont Mary ultramylonite showing the typical microstructure, including a dark mica-rich matrix and white recrystallised quartz-plagioclase ribbons. The red arrows indicate examples of plagioclase (left) and garnet (right) porphyroclasts.

Figure 2 *Mechanical data for the experiment S1771. A) Friction coefficient and equivalent slip rate versus equivalent displacement. B) Friction coefficient and normal stress versus time.*

Figure 3 One-to-one comparison between (A) natural and (B) experimental pseudotachylyte. In the lower right-hand side of both images, host-rock garnet marks the boundary of the pseudotachylyte. Notice that host-rock garnet is intensely comminuted in the natural case (A), while it is mostly intact in the experimental one (B). Dark clasts (quartz and sillimanite) are clearly the dominant ones in both veins; lighter gray plagioclase clasts are present in both, but clearly less abundant; while bright garnet clasts are only present close to the vein border in proximity of host-rock garnet. In (B), brightest small crystals, abundant toward the upper border of the vein and absent in the centre, are ilmenite clasts.

Figure 4 *SEM-BSE images of microstructures of garnet clasts in the experimental pseudotachylyte (sample S1771). A) An isolated garnet clast surrounded by a light-coloured matrix. B) Cluster of garnet clasts close to the vein border. Abundant vesicles (black bubbles) are visible in (A) and (B), possibly due to emission of gas released by melting of phyllosilicates. C-D) Garnet fragmented down to the submicrometric scale at the contact between host-rock garnet and melt. Chemical analysis of the fragments in (D) in Figure S1. E) Host-rock large garnet porphyroclast crosscut by the pseudotachylyte vein.*

Figure 5 Volume percent abundances in host rock and survivor clasts in pseudotachylyte for quartz, plagioclase, sillimanite, and garnet. Data for the host rock are the average between the rotary and stationary sample (Table 1), under the hypothesis that both samples melt equally during the experiment. HM stands for high-magnification (30-50 pixels/μm) maps, LM for low-magnification (8.5 pixels/μm) maps. HM are the average of six maps; LM of four maps (Table 2).

Figure 6 SEM-BSE images of the experimental pseudotachylyte with location of the element maps. In SEM-BSE images the host rock is blackened and garnet survivor clasts are highlighted in red. Chemical maps are false-colour images obtained by combination of element maps of Si, Al, Ca, and Fe each with a different colour. Quartz results reddish, sillimanite blue, plagioclase yellow/orange, and garnet light blue.

Figure 7 Example of bitmaps created from element map 90 (see Fig. 2). A) SEM-BSE image of the area corresponding to the map. B) False-colour image obtained by combination of element maps of Si, Al, Ca, and Fe. On the left-hand-side the element maps for (C) Al, (E) Na, and (G) Si. On the right-hand-side the corresponding bitmaps created from the element maps for (D) sillimanite, (F) plagioclase, and (H) quartz.

Figure 8 Clast size distributions (CSDs) in the experimental pseudotachylyte. HM stands for high-magnification (30-50 pixels/μm) maps, LM for low-magnification (8.5 pixels/μm) maps. D_{2D} is the slope of the linear fit of the curve in the range in which the coefficient of correlation R^2 is greater than 0.99. A-C) CSD of sillimanite (A), plagioclase (B), and quartz (C) in LM maps. D) Comparison between CSD of sillimanite and plagioclase in HM maps.

Table 1 Modal abundances of minerals in host rock obtained by X-Ray Powder Diffraction. S1771R is the rotary sample, S1771S the stationary sample.

Table 2 Modal abundances of minerals in pseudotachylyte clasts obtained by image analysis on element maps of Si, Al, Ca, and Fe. Average values are shown for the high-magnification (HM) and low-magnification (LM) maps.

Table 1

Minerals	***S1771R*** % vol	***S1771S*** % vol
Quartz	42.1	47.2
Plagioclase	14.5	9.8
Sillimanite	7.5	8.2
Garnet	4.1	3.1
Subtotal	***68.2***	***68.2***
Biotite	19.2	18.5
Muscovite	8.3	9.5
Chlorite	3.8	3.2
Ilmenite	0.6	0.4
Total	**100.1**	**99.9**

Table 2

Chemical map #	***Resolution*** pixel/µm	***Area*** μm^2	***Quartz*** % vol	***Sillimanite*** % vol	***Plagioclase*** % vol	***Garnet*** % vol	***All clasts*** % vol
92	50.6	1229	19.3	2.5	2.8	0.0	24.5
26	33.7	2770	21.2	1.8	1.4	0.0	24.4
27	33.7	2770	21.4	2.0	4.0	0.0	27.4
94	33.7	2770	23.8	3.0	1.8	0.0	28.7
98	33.7	2770	23.2	2.4	3.7	0.0	29.4
96	29.6	3581	28.8	5.3	1.6	0.0	35.6
HM maps			***23.0 ± 1.3***	***2.8 ± 0.5***	***2.6 ± 0.5***	***0.0***	***28.3 ± 1.7***
85	8.5	38615	21.6	3.6	2.1	0.0	27.4
86	8.5	35087	25.1	3.7	0.6	0.1	29.5

88	8.5	32914	26.5	4.2	1.1	0.0	31.7
90	8.5	35047	18.3	3.2	0.7	0.4	22.5
LM maps			***22.8 ± 1.6***	***3.7 ± 0.6***	***1.1 ± 0.6***	***0.1***	***27.7 ± 2.1***

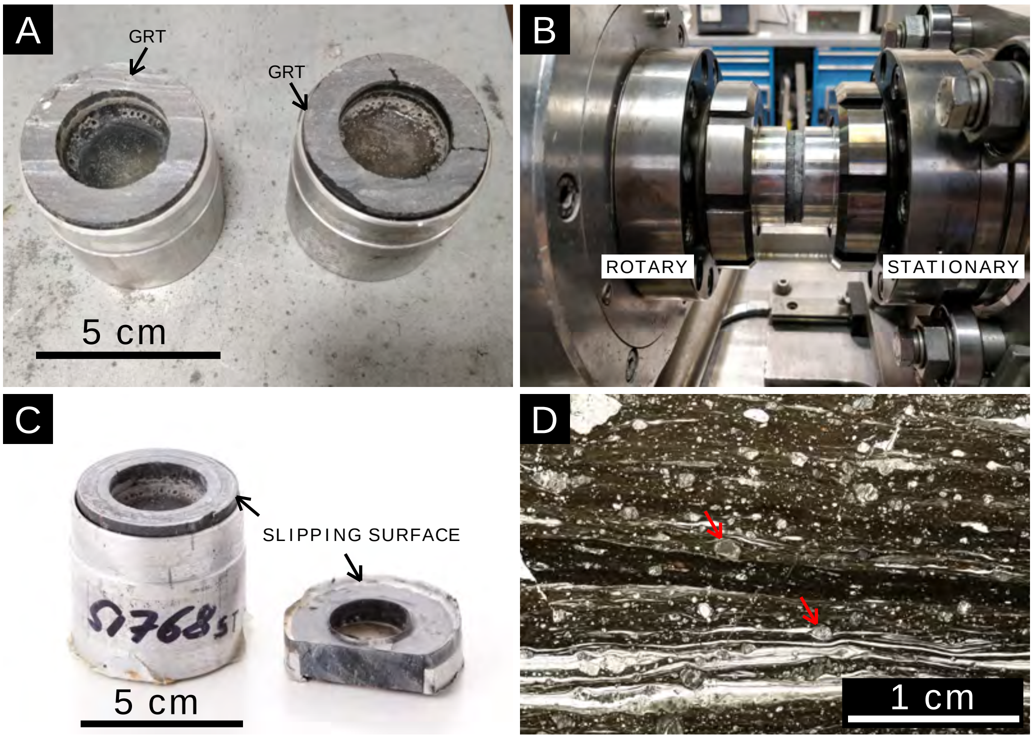
A
GRT
GRT
5 cm
B
ROTARY
STATIONARY
C
SLIPPING SURFACE
S1768ST
5 cm
D
1 cm

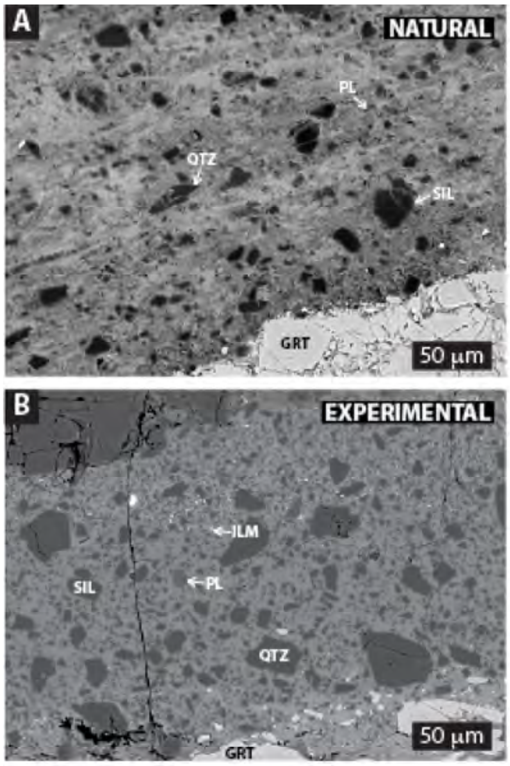
A
NATURAL
PL
QTZ
SIL
GRT
50 μm
B
EXPERIMENTAL
ILM
SIL
PL
QTZ
GRT
50 μm

FIGURE 1

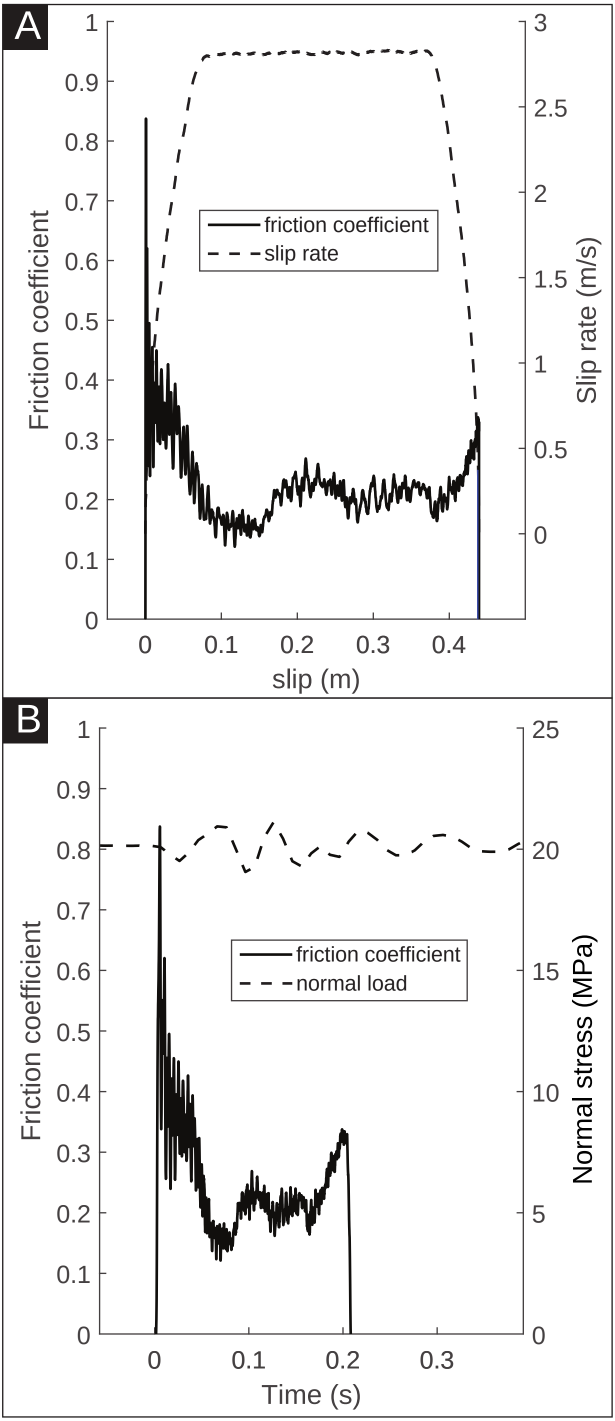
A
Friction coefficient
Slip rate (m/s)
friction coefficient
slip rate
slip (m)
0
0.1
0.2
0.3
0.4
0.5
0.6
0.7
0.8
0.9
1
0.5
1.5
2
2.5
3
B
Friction coefficient
Normal stress (MPa)
friction coefficient
normal load
Time (s)
5
10
15
20
25

FIGURE 4

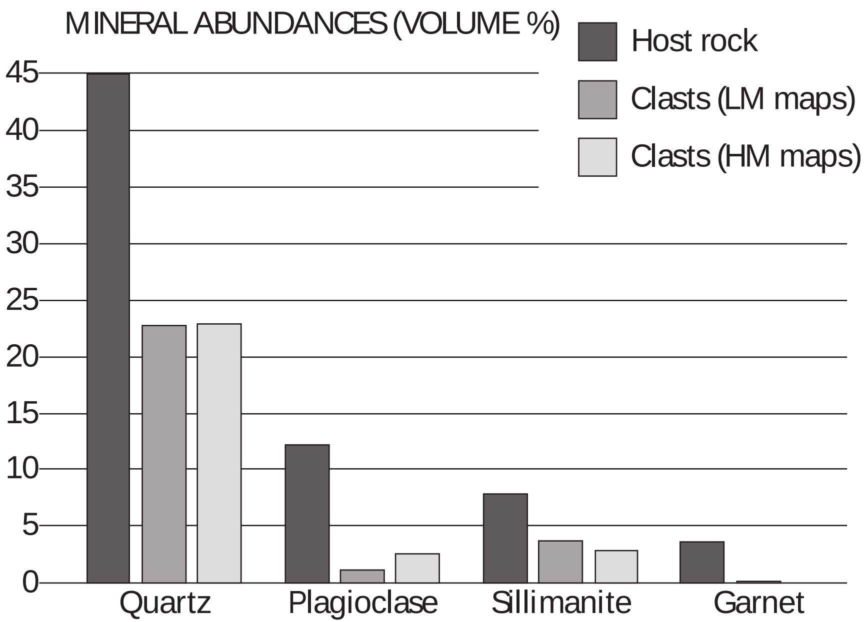

Mineral	Host rock	LM maps	HM maps
Quartz	44.6	22.8	23.0
Plagioclase	12.1	1.1	2.6
Sillimanite	7.8	3.7	2.8
Garnet	3.6	0.1	0.0
Total	68.2	27.7	28.3

FIGURE 6

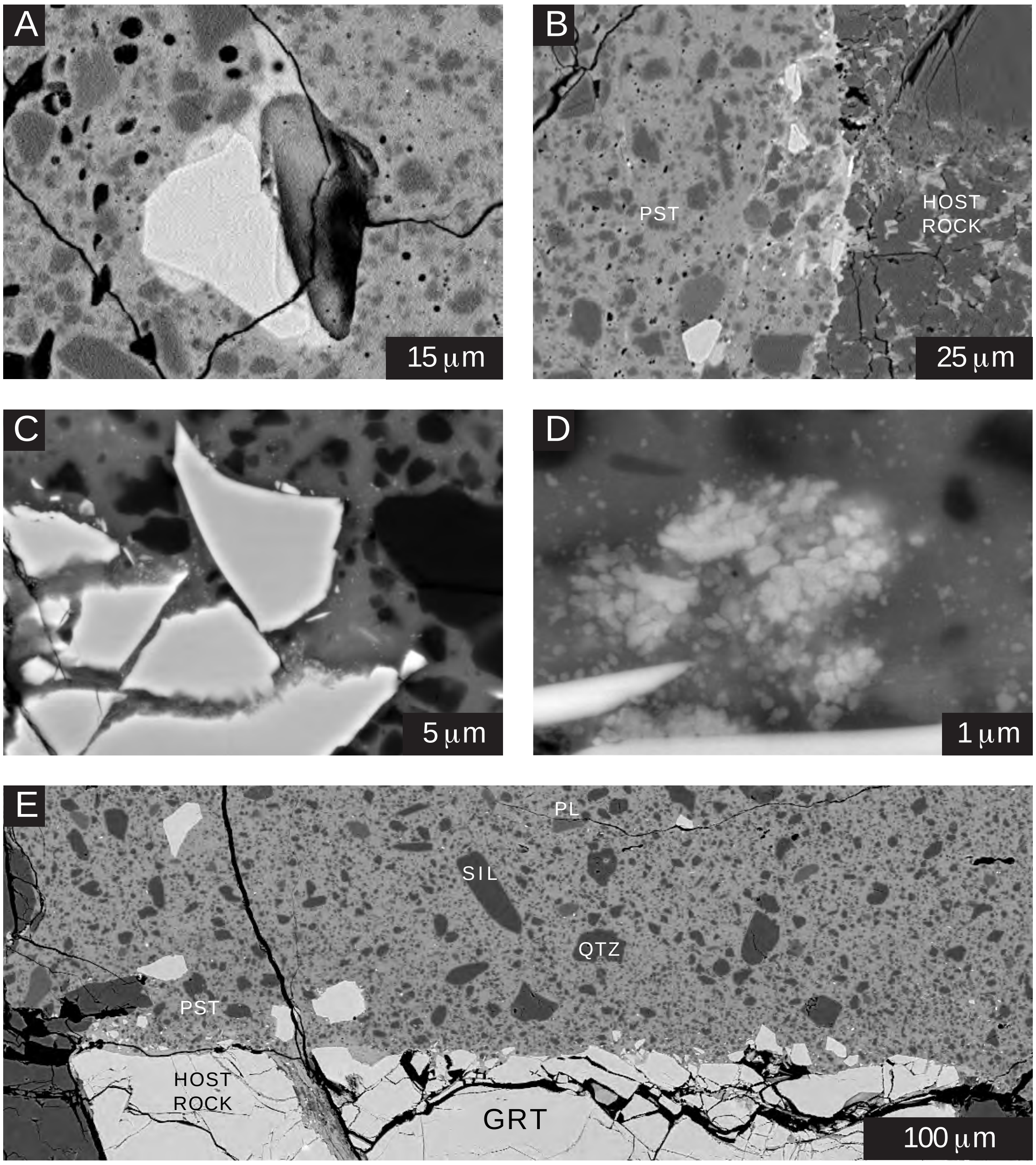
A
15 μm
B
PST
HOST ROCK
25 μm
C
5 μm
D
1 μm
E
PL
SIL
QTZ
PST
HOST ROCK
GRT
100 μm

FIGURE 5

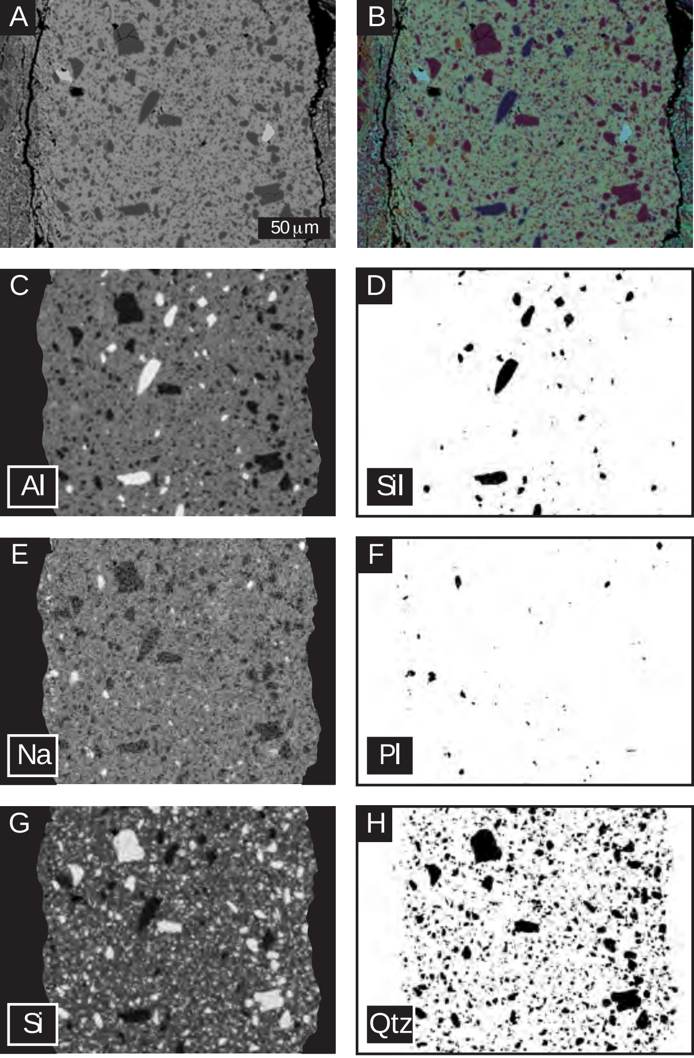

FIGURE 3

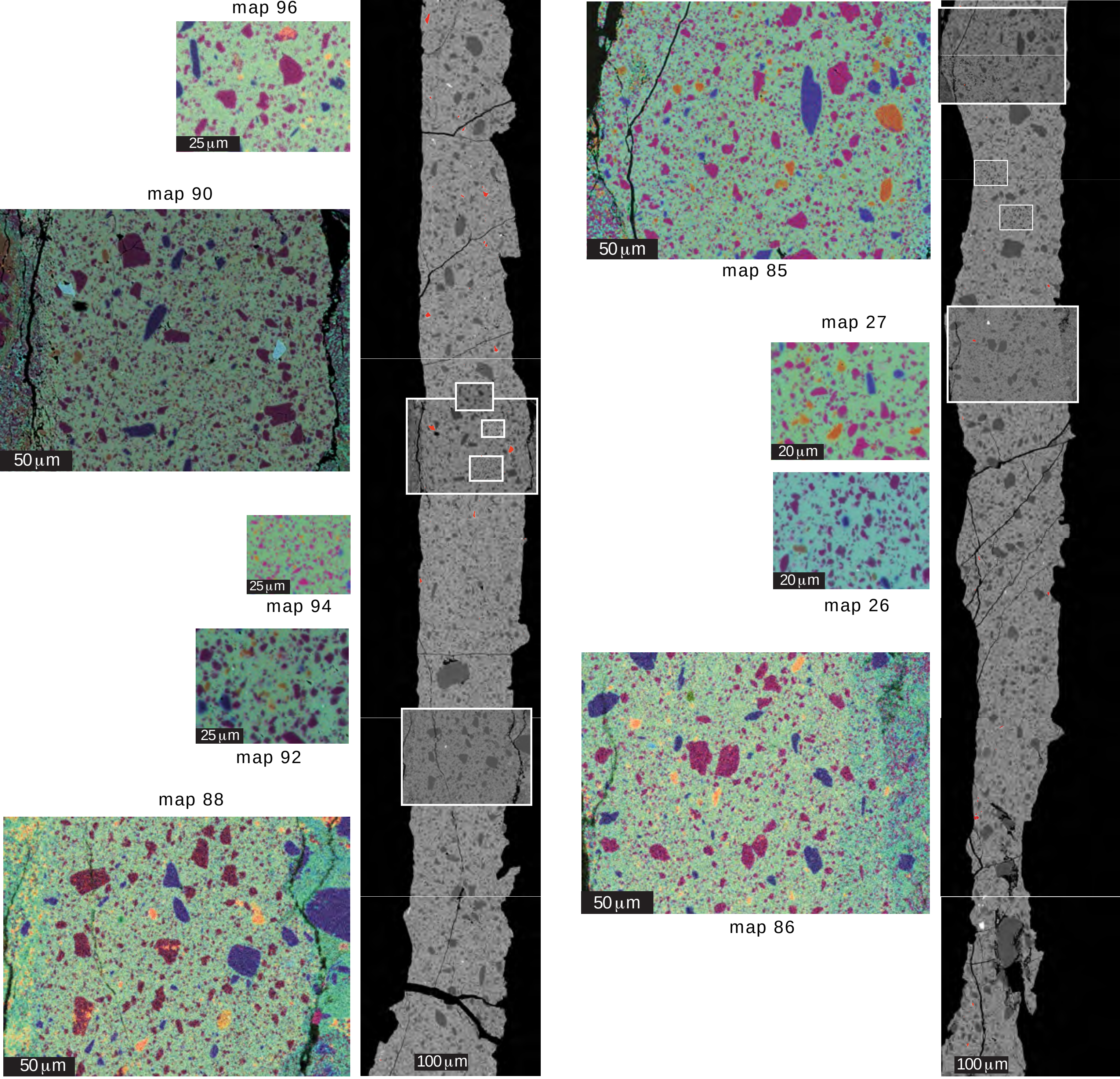
map 96
25 µm
map 90
50 µm
25 µm
map 94
25 µm
map 92
map 88
50 µm
100 µm
50 µm
map 85
map 27
20 µm
20 µm
map 26
50 µm
map 86
100 µm

FIGURE 2

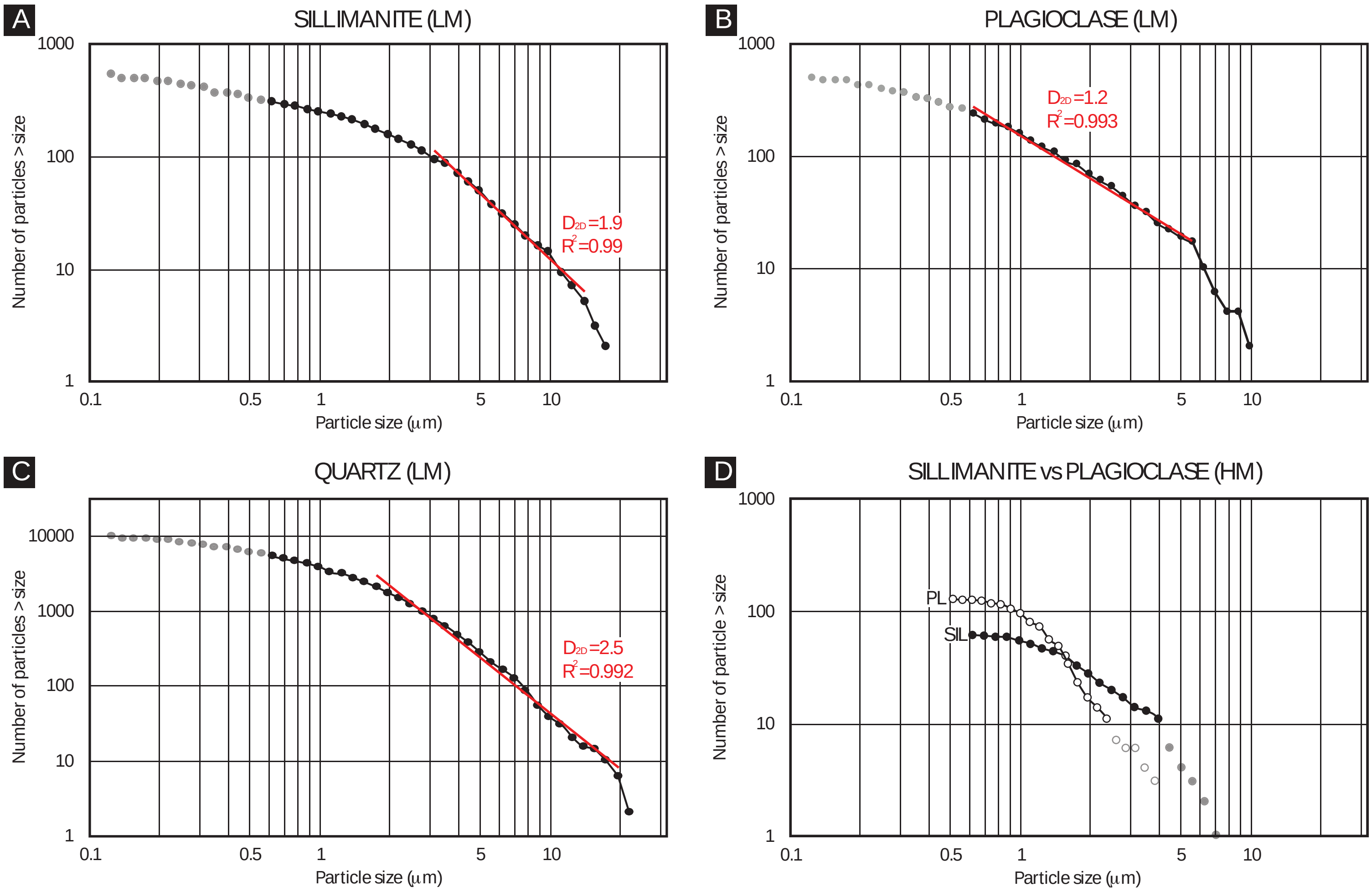
A
SILLIMANITE (LM)
D2D=1.9
R2=0.99
B
PLAGIOCLASE (LM)
D2D=1.2
R2=0.993
C
QUARTZ (LM)
D2D=2.5
R2=0.992
D
SILLIMANITE vs PLAGIOCLASE (HM)
PL
SIL
Number of particles > size
Number of particle > size
Particle size (μm)

FIGURE 7

Figure S1: Chemical point analyses and chemical transect in the area of figure 5D (sample S1771).

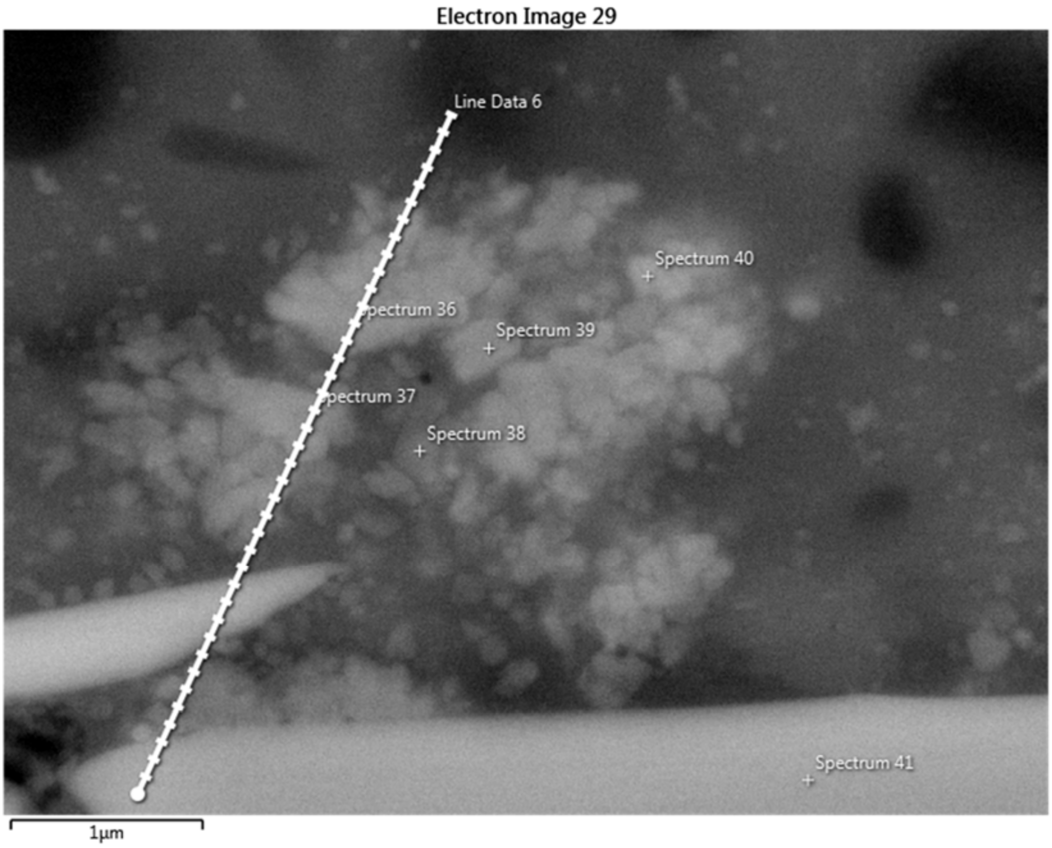

% oxides	#36	#37	#38	#39	#40	**#41 (hr-grt)**
SiO_2	48.8	48.4	35.5	33.2	36.5	**36.3**
FeO	20.0	19.1	23.4	25.7	23.8	**33.7**
Al_2O_3	15.5	16.8	24.2	20.4	21.5	**22.6**
K_2O	1.9	2.2	2.3	1.4	1.7	**0.7**
MgO	13.1	12.6	13.8	18.9	15.6	**4.6**
TiO_2	0.3	0.5	0.5	0.0	0.5	**0.0**
CaO	0.3	0.4	0.4	0.3	0.4	**1.3**
MnO	0.0	0.0	0.0	0.0	0.0	**0.8**

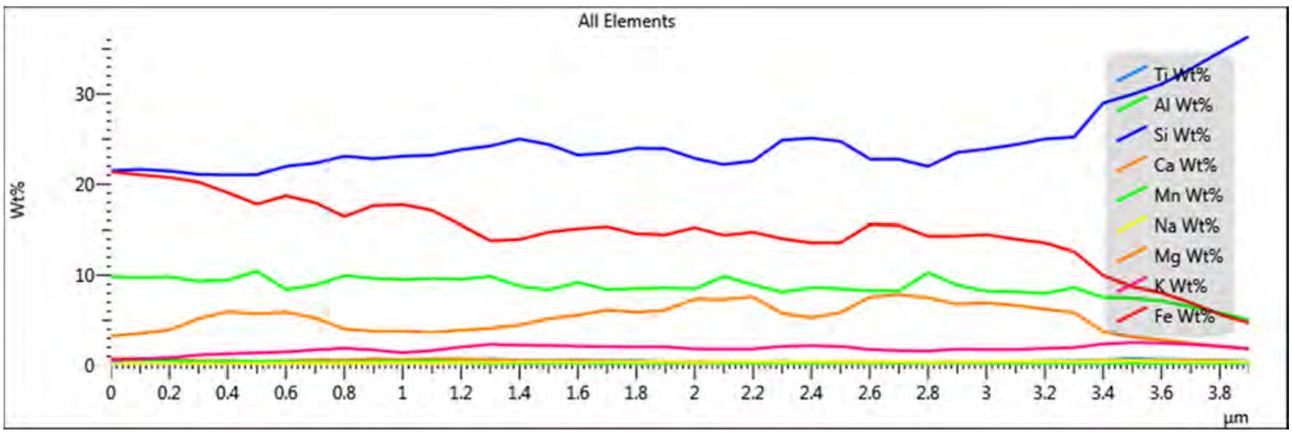

Figure S2: Chemical composition along a transect across a 100 nm microlite (sample S1771). Due to the small size with respect to the spot size, a chemical analysis of the microlite was not possible, but the transect clearly shows that an enrichment in Al, Mg, and Fe with respect to the matrix.

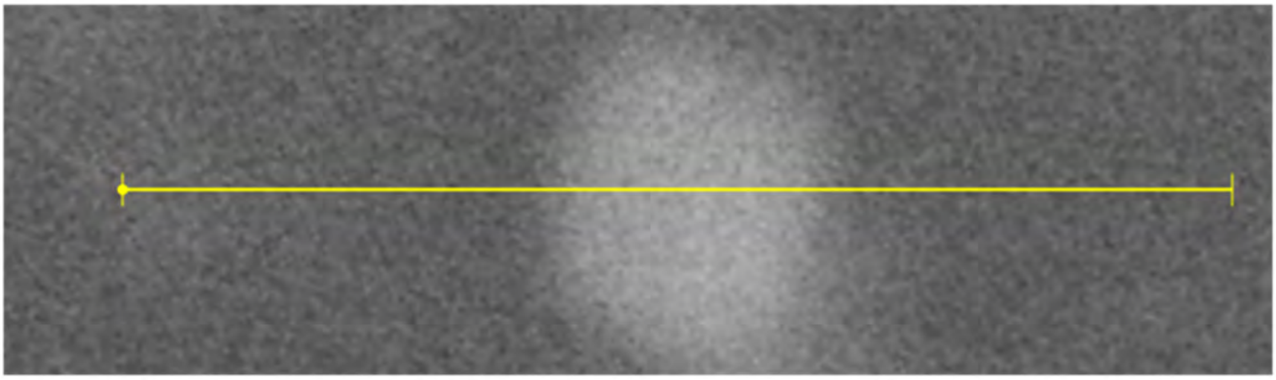

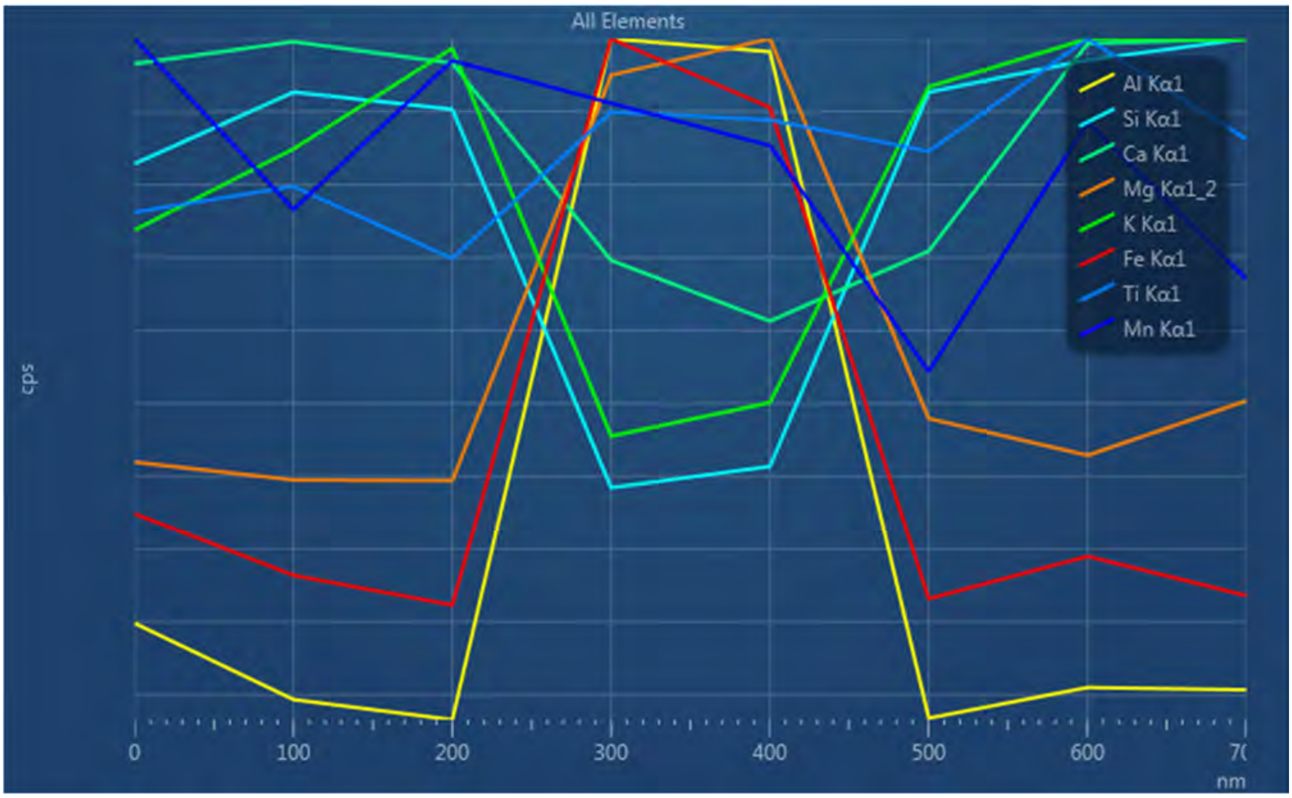

Table S1: Thermomechanical properties of rock forming minerals. $\boldsymbol{K_{IC}}$ is the mode I fracture toughness; $\boldsymbol{E_B/E_{LIMIT}}$ is a measure of the energy efficiency of comminution (Tromans, 2008); $\boldsymbol{R}$ is the resistance to thermal shock as proposed by Papa et al. (2018); $\boldsymbol{T_{melting}}$ is the single-mineral melting temperature as discussed in section *4.1* of the main text.

Resistance to thermal shock $\boldsymbol{R}$, can be written in a general form as $R = \frac{k\,Kc}{\alpha\,K}$ (e.g. Kingery et al., 1955), where $\boldsymbol{k}$ is the thermal conductivity, K_c is the fracture toughness, α is the thermal expansion parameter, and K is the bulk modulus. Garnet low resistance to thermal shock mainly results from a combination of high bulk modulus (that causes high thermal stresses) and low thermal conductivity. Thermal conductivity $\boldsymbol{k}$ is an important parameter since, as already observed by Spray (1992), minerals with low $\boldsymbol{k}$ are more susceptible to thermal shock because they have to withstand steeper thermal gradients at their margin.

Minerals	$\boldsymbol{K_{IC}}$ **(MPa m$^{1/2}$)**	$\boldsymbol{E_B/E_{LIMIT}}$ **(%)**	$\boldsymbol{R}$ **(W m$^{-1/2}$ x10^{-3})**	$\boldsymbol{T_{melting}}$ **°C**	***k**** ***(W m^{-1} K^{-1})***
Garnet	1.31 [1]	11.0 (Grossular) [3]	0.51 [4]	1200 [5]	1.5 [6]
Plagioclase (An_{35})	0.75 [1]	11.7 (Anorthite) [3]	0.82 [4]	1200-1400 [5]	1.7 [7]
Quartz	1.50 [2]	14.8 [3]	1.51 [4]	1700 [5]	7.2 [7]
Sillimanite	1.60 [2]	-	2.40 [4]	1600-1850 [5]	9.0 [7]
Muscovite/Biotite	0.2 [7]	-	-	700-900 [5]	1.7-2.5

* At 20 °C and 1 atm.

1. Tromans, D., and Meech, J. A., 2002, Fracture toughness and surface energies of minerals: theoretical estimates for oxides, sulphides, silicates and halides: *Minerals Engineering*, v. 15, p. 1027-1041.
2. Whitney, D. L., Broz, M., and Cook, R. F., 2007, Hardness, toughness, and modulus of some common metamorphic minerals: *American Mineralogist*, v. 92, p. 281-288.
3. Tromans, D., 2008, Mineral comminution: Energy efficiency considerations: *Minerals Engineering*, v. 21, p. 613-620.
4. Papa, S., Pennacchioni, G., Angel, R. J., & Faccenda, M. (2018). The fate of garnet during (deep-seated) coseismic frictional heating: The role of thermal shock. *Geology*, *46*(5). https://doi.org/10.1130/G40077.1
5. see discussion and references in section 4.1, main text
6. Kanamori, H., Fujii, N., and Mizutani, H., 1968, Thermal diffusivity measurement of rock-forming minerals from 300 to 1100 K: *Journal of geophysical research*, v. 73, p. 595-605.
7. Spray, J., 2010, *Annu. Rev. Earth Planet. Sci.* 2010. 38:221–54